Electrochemical Science Advances

WILEY-VCH

ELECTROCHEMICAL SCIENCE ADVANCES Open Access

RESEARCH ARTICLE OPEN ACCESS

How Microstructures, Oxide Layers, and Charge Transfer Reactions Influence Double Layer Capacitances. Part 2: Equivalent Circuit Models

Maximilian Schalenbach[1] | Luc Raijmakers[1] | Hermann Tempel[1] | Rüdiger-A. Eichel[1,2]

[1]Fundamental Electrochemistry (IEK-9), Institute of Energy and Climate Research, Forschungszentrum Jülich, Jülich, Germany | [2]Institute of Physical Chemistry, RWTH Aachen University, Aachen, Germany

Correspondence: Maximilian Schalenbach (m.schalenbach@fz-juelich.de)

Received: 7 May 2024 | **Revised:** 15 July 2024 | **Accepted:** 17 July 2024

Funding: This work was supported by the German Federal Ministry of Education and Research (BMBF) within the Project PhasKat (033RC028E).

ABSTRACT

In the first part of this study, double layer (DL) capacitances of plane and porous electrodes were related to electrochemical active surface areas based on electrochemical impedance spectroscopy (EIS) and cyclic voltammetry (CV) measurements. Here, these measured data are described with equivalent circuit models (ECMs), aiming to critically assess the ambiguity, reliability, and pitfalls of the parametrization of physicochemical mechanisms. For microstructures and porous electrodes, the resistive–capacitive contributions of DL in combination with resistively damped currents in pores are discussed to require the complexity of convoluted transmission line ECMs. With these ECMs, the frequency-dependencies of the capacitances of porous electrodes are elucidated. Detailed EIS or CV data-based reconstructions of complex microstructures are discussed as impossible due to the blending of individual structural features and the related loss of information. Microstructures in combination with charge transfer reactions and weakly conducting parts require parameter-rich ECMs for an accurate physicochemical description of all physicochemical mechanisms contributing to the response. Nevertheless, the data of such a complex electrode in the form of an oxidized titanium electrode are fitted by an oversimplistic ECM, showing how easily unphysical parameterizations can be obtained with ECM-based impedance analysis. In summary, trends in how microstructures, charge transfer resistances and oxide layers can influence EIS and CV data are shown, while awareness for the overinterpretation of ECM-analysis is raised.

1 | Introduction

The first experimental and theoretical examinations on the double layer (DL) date back to 1879 by Helmholtz [1]. Major contributions of Gouy [2], Chapman [3] and Stern [4] followed in the beginning of the 20th century, who developed electrostatics models for the ion distribution in the DL. In the 1940s, Grahame [5, 6] was among the first researchers who probed DL responses under varying potentials, describing the DL as a capacitance. However, DL responses typically show frequency-independent phase angles that are higher than the −90° of a capacitor (see the first part of this study [7]). In 1984, Brug et al. [8] introduced a constant phase element (CPE) to give a more precise description of electrochemical impedance spectroscopy (EIS) data on DLs. Afterwards, the DLs of plane electrodes were typically represented with CPEs in equivalent circuit models (ECMs) [9–15].

Abbreviations: CPE, Constant phase element; CT, Charge transfer; CTL, Convoluted transmission line; CV, Cyclic voltammetry; DL, Double layer; ECM, Equivalent circuit model; EIS, Electrochemical impedance spectroscopy; TL, Transmission line.

However, as recently reviewed by Huang et al. [16], for ECMs for porous electrodes, DLs are often parameterized by capacitances for the sake of simplification.

In 1964, De Levie [17] reported a transmission line (TL) ECM to describe the electrochemical impedance of pores without charge transfer reactions. These TLECMs consist of a ladder network of resistances and capacitances, which represent the ohmic drop of the ion conduction in the pore and the DL capacitance, respectively. Until today, this TL-ECM is commonly used in the literature [16, 18, 19] to describe porous electrodes. In some works [20–26], resistances of the electron conduction in the solid phase of the electrode are added to the TC-ECM. In 2000, Bisquert [27] first reported a TL-ECM for pores in which the DL is represented by CPEs instead of capacitances, which agrees better with the measured CPE-type DL responses of plane electrodes. However, this approach was used in only a few of the following works [16, 28–31]. The traditional electrostatic approaches to model the differential capacitance of the DL were also applied to porous electrodes [32, 33]. However, such models cannot describe the electrodynamics of the resistive–capacitive ion transport under an alternating potential and are not helpful for the design of ECMs.

Wang [34] reported in 1987 that a CPE can be described by an infinite TL-ECM. Based on Wang's pioneer work, the physicochemical causes for the CPE-type appearance of the DL at plane electrodes were recently explained by its TL counterpart [35, 36]. In detail, the TL-ECM can describe the infinitesimal resistive and capacitive contributions of the ion displacement in the DL. With reference to Wang's interpretation of the CPE as a TL [34], Bisquert's TL with CPEs for the DL thus describes a convoluted transmission line (CTL), consisting of TLs for the intrinsic properties of the DL and the porous electrode structure, respectively. Similarly appearing CTL-based ECMs (CTL-ECMs) were also used to describe hierarchical type of pores [19, 37–39], yet with capacitances representing the DL. To calculate TL responses, mostly analytical approaches were presented in the literature [40–42], in which the parameterization of the ECMs is limited to boundary conditions of the analytical calculus. Scientifically, the response of the DL in porous structures to alternating potentials (as such applied during EIS or CV) with the resistive–capacitive coupling of the ion transport is not well understood. A systematic experimental characterization of porous electrodes in comparison to simulated data of thoughtfully chosen ECMs is missing in the literature.

The aim of the second part of this study is to provide a deeper understanding of the effect of resistive–capacitive ion transport in porous electrodes on the frequency dependence of the DL capacitance. In addition, the influences of morphologies, oxide layers, and charge transfer reactions on the DL capacitance are simulated and compared to the measured EIS and CV data presented in the first part of this study [7]. Based on 50 years of literature on ECMs describing cracks, pores and porous structures, Bisquert's CTL-ECM approach is further developed and extended. A mixed analytical–numerical procedure to simulate the EIS and CV data of the developed ECMs is introduced to overcome the limitations and boundary conditions of the thus far reported purely analytical solutions of CTLs. With reference to the direct comparison of the measured responses from the first part of this study and the simulated responses of ECMs, challenges and pitfalls of the EIS and CV data-based parameterization are critically discussed. The source codes of all the presented calculations are supplied in Supporting Information section, proving a powerful toolbox to calculate the impedance data on CTL-ECMs.

2 | Methods and Model Development

The aim of this section is to present and elucidate ECMs that describe the influence of microstructures, oxide layers, and charge transfer reactions on EIS and CV data. Hereto, the ECMs introduced in Section 1 are reviewed and improvements are presented. Subsequently, methods to calculate the impdances of the presented ECMs are discussed. Finally, remarks on the parameterization of pores are discussed.

2.1 | ECMs for Microstructures

Figure 1 shows ECMs for simulating the DL response. Figure 1A shows the ECM typically used for a plane electrode [9–15, 43], consisting of a resistance for the liquid electrolyte phase R_{liq}, a resistance for the electronic conductivity in the solid phase R_{sol}, and a CPE Z_{CPE} to describe the DL. The resistances R_{liq} and R_{sol} can be combined to form one resistance. This combined resistance was defined as serial resistance R_{s} in the first part of this study. This ECM serves here as a reference, from which the features coming from conductivity-limiting electrode morphologies deviate.

Figure 1B shows De Levie's [17] TL-based ECM that aims to represent a straight-wall pore. In this circuit, the DL is parameterized by capacitances that are arranged along the pore. The individual capacitances C^k are connected by resistances R^k_{liq} that account for the ionic resistance of the electrolyte in the pore. The superscripts of the resistances and capacitances denote the ladder step k, ranging from 0 to the maximum ladder step L. Figure 1C shows Bisquert's [27] ECM, where the capacitances of De Levie's TM-ECM are replaced by CPEs with the impedance

$$Z^k_{\mathrm{CPE}} = \frac{\xi}{(i\,2\pi\,f)^n}, \tag{1}$$

where f denotes the frequency, i the complex number, ξ the CPE prefactor, and n the CPE exponent. With reference to the interpretation of a CPE by a TL-ECM (see Section 1), this ECM is here interpreted as a convoluted tranmission line (CTL). In addition to Bisquert's [27] original CTL-ECM, the ECM in Figure 1C shows resistances $\tilde{R}^k_{\mathrm{sol}}$ for the electron conduction in the solid phase, which were introduced by several authors [20–26] for De Levie's TL-ECM.

Figure 1D shows a similar ECM as Figure 1C, however, the resistances $\tilde{R}^k_{\mathrm{sol}}$ of the solid phase are rearranged to ease the below presented calculus for the impedance. In this arrangement, the resistances R^k_{sol} of the solid phase are calculated as a function of the resistances $\tilde{R}^k_{\mathrm{sol}}$ from the ECM in Figure 1C by:

$$R^k_{\mathrm{sol}} = \sum_{i=k}^{L} \tilde{R}^i_{\mathrm{sol}}. \tag{2}$$

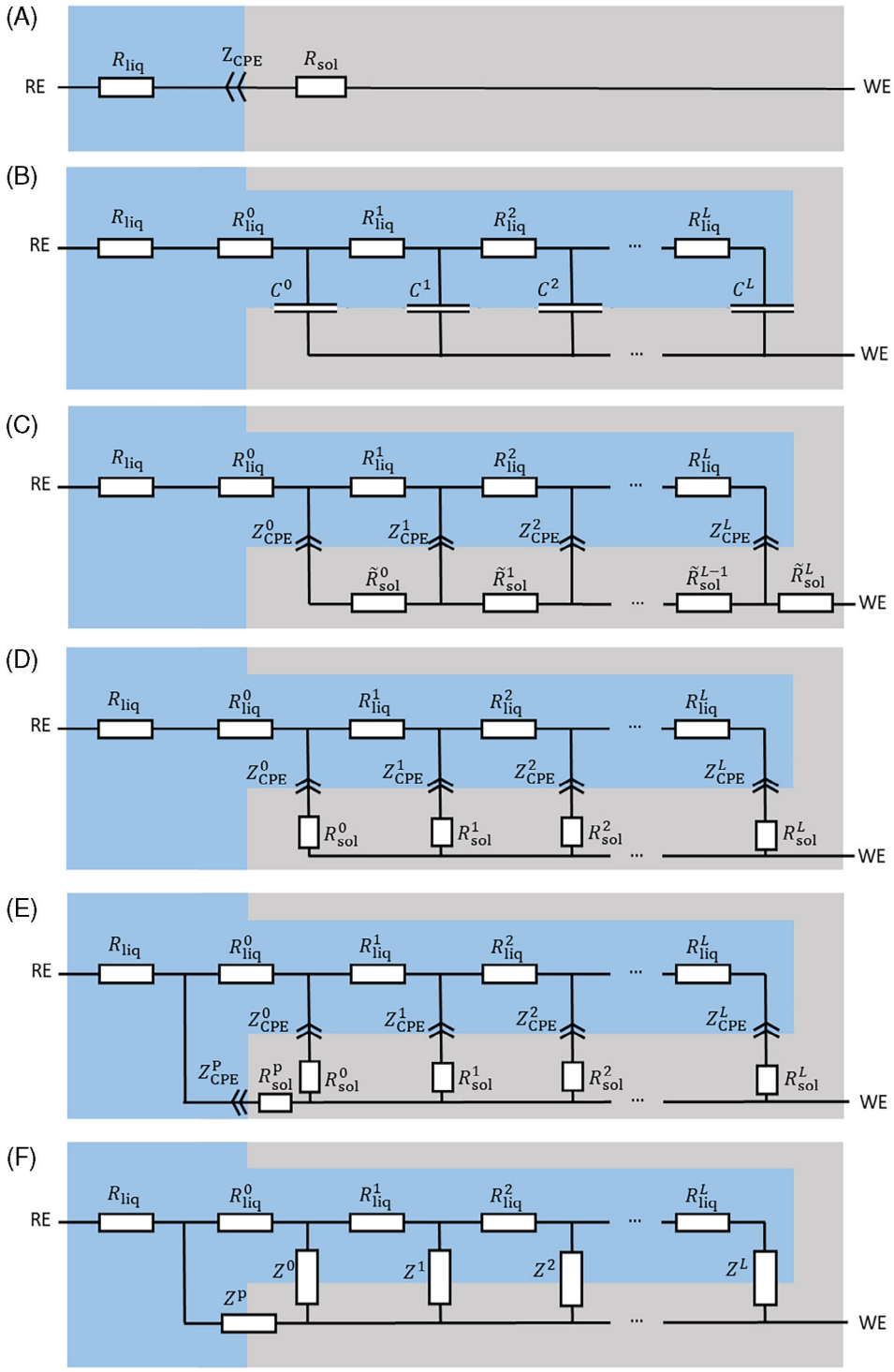

FIGURE 1 | Equivalent circuit models (ECMs) for a plane electrode (A) and a pore (B–F). Blueish shaded areas: electrolytic phase. Greyish shaded areas: solid phase. (A) ECM for a plane electrode, consisting of a resistance for the electrolyte (R_{liq}), a resistance for the solid phase (R_{sol}), and constant phase element (Z_{CPE}) for the double layer. (B) De Levie's [17] classical transmission line model for a pore. (C) Bisquert's [27] transmission line, for which the infinitesimal double layers are represented by constant phase elements (CPEs). Moreover, resistances for the solid phase are added. (D) Rearrangement of the resistances of the solid phase for easier calculation. (E) ECM of the pore plus the resistance and double layer of the plane part of the electrode. (F) Generalized ECM for a pore with arbitrary electrochemical processes (described by the impedance Z^k) at the electrolyte-solid interface.

In the circuit of Figure 1E, the properties of the plane electrode are added to the CTLECM with a resistance R_{sol}^p and a CPE Z_{CPE}^p. This approach is adopted from Bosch et al. [44], who similarly described a plane electrode with cracks and pores. Hence, the plane properties basically represent one more ladder step in the CTL. However, the parameter values of the plane contributions (R_{sol}^p and Z_{CPE}^p) are expected to strongly deviate from the parameter values of the CTL in the pores (R_{sol}^k and Z_{CPE}^k) due to different conductivities, surface areas, ion movements, and electric field penetrations depths.

Figure 1F shows a generalized ECM for the TL [41, 45], in which the impedances at the electrochemical interfaces can be replaced by arbitrary impedances Z^k. Applying the analytical calculation procedure described by Wang [34] for De Levie's TL-ECM to the CTL-ECM, its impedance Z_{CTL} can be calculated by a continuous fraction in the form of:

$$Z_{\mathrm{CTL}} = R^0_{\mathrm{liq}} + \cfrac{1}{\frac{1}{Z^0} + \cfrac{1}{R^1_{\mathrm{liq}} + \frac{1}{Z^1} + \cfrac{1}{R^2_{\mathrm{liq}} + \frac{1}{Z^2} + \cdots}}}. \tag{3}$$

The total impedance $Z_{1\mathrm{F}}$ of the circuit in Figure 1F can then be calculated by adding one more element to the TL, which leads to:

$$Z_{1\mathrm{F}} = R_{\mathrm{liq}} + \frac{1}{\frac{1}{Z^p} + \frac{1}{Z_{\mathrm{CTL}}}}. \tag{4}$$

2.2 | ECMs for Oxide Layers and Charge Transfer Reactions

The above-discussed ECMs are directly applicable to describe the response of electrodes without charge transfer reactions and without oxide coverage. The differences of the electronic structure of metals and semi-conducting or insulating oxide coverage are reported to affect the DL capacitance [46–48]. The physicochemical effect of electronic interactions on the parameterization is beyond the scope of this study, which focuses on the empirical parameterization and validation of the ECMs. The circuit of Figure 1F allows to incorporate arbitrary impedances models for the electrochemical electrolyte–electrode interface. Figure 2 shows some examples of ECMs for this interface and the resistance of the solid phase. The electrolyte resistance is excluded, so that the interface models can be directly inserted into the ECM of Figure 1F.

Figure 2A shows the interface model of the DL for an inert and oxide-free electrode. The total impedance $Z_{2\mathrm{A}}$ of this series connection equals the sum of $Z_{\mathrm{CPE_{DL}}}$ for the CPE that describes the DL and the resistance R_{sol} of the solid phase:

$$Z_{2\mathrm{A}} = Z_{\mathrm{CPE_{DL}}} + R_{\mathrm{sol}}. \tag{5}$$

The ECM of Figure 2B includes diffusion-limited charge transfer processes parallel to the DL for an oxide layer-free electrode. The CPE-based impedance $Z_{\mathrm{CPE_{CT}}}$ describes diffusion limitations of the charge transfer [37]. The resistance of the charge transfer reaction itself is described by R_{CT}. The total impedance $Z_{2\mathrm{B}}$ of this ECM equals:

$$Z_{2\mathrm{B}} = \frac{1}{\frac{1}{Z_{\mathrm{CPE_{DL}}}} + \frac{1}{Z_{\mathrm{CPE_{CT}}} + R_{\mathrm{CT}}}} + R_{\mathrm{sol}}. \tag{6}$$

Figure 2C shows an ECM for an oxide-covered electrode without charge transfer reactions, resembling an inert oxide coverage. Again, the DL is described by a CPE. Following Medway et al. [49], the oxide layer is described by a capacitor C_{ox}, which accounts for the capacitive properties of a low-conducting or insulating oxide layer. A parallel resistor $R_{\mathrm{ox,p}}$ is added to this capacitance, which accounts for leakage currents that arise from the oxide's conductivity [50, 51]. Hence, capacitive charge contributions and electron conduction of the oxide layer are described by the ECM. In addition, a serial resistor $R_{\mathrm{ox,s}}$ represents a resistance in series to the leaky capacitor. The total impedance $Z_{2\mathrm{C}}$ of this circuit equals:

$$Z_{2\mathrm{C}} = Z_{\mathrm{CPE_{DL}}} + \frac{1}{i\,(2\pi f C_{\mathrm{ox}}) + \frac{1}{R_{\mathrm{CT}}}} + R_{\mathrm{ox,s}} + R_{\mathrm{sol}}. \tag{7}$$

The ECM for the electrochemical interface in Figure 2D describes an oxide-covered electrode at which diffusion-limited charge transfer reactions appear, combining the circuits of Figure 2B,C. The total impedance $Z_{2\mathrm{D}}$ of the resulting ECM equals the sum of the impedance $Z_{2\mathrm{B}}$ and $Z_{2\mathrm{C}}$ (R_{sol} is deducted to not account for twice for the resistance of the solid phase):

$$Z_{2\mathrm{D}} = Z_{2\mathrm{B}} + Z_{2\mathrm{C}} - R_{\mathrm{sol}}. \tag{8}$$

2.3 | Computational Calculations

A computational framework to calculate the impedance of CTL-ECMs was programmed in the language Python, for which the source codes are supplied in the Supporting Information section to this article. In this framework, the impedances of the ladder steps of the CTL are calculated analytically. To compute the total impedance of the CTL-ECM by Equation (3), the complex impedances of each of these ladder steps are added numerically in an iterative process that starts at the last step of the ladder and ends at the first ladder step. CV data are simulated based on a recently published impedance-based inverse Fourier transform model [43]. In brief, with this approach, a Fourier series expresses the harmonic content of the triangular potential variation during CV, for which the impedances are individually calculated in the time domain. The currents derived from the impedances of the individual harmonic contents are summed up in the time domain to obtain simulated CV data.

2.4 | Remarks and Examples on the Parameterization of Pores

In the Supporting Information, the work of Wang [34] is briefly reviewed and discussed, showing sets of resistances R^k_{liq} and capacitances C^k in a TL-ECM (shown in Figure 1B) that resemble the response of CPEs. Such TLs were discussed as a physicochemical interpretation of the DL response [35, 36] and their CPE-like appearances [43]. With the CPE-like parameterization of the TL, the resistances R^k_{liq} increase, whereas the capacitances C^k decrease towards higher ladder steps (graphed in the Supporting Information). In a TL with such a CPE-like parameterization, the current eventually declines towards larger ladder steps [35]. In the case of a short and wide pore, however, the resistive damping has a little impact on the capacitive currents of the pore so that the entire surface of the pore contributes to the DL response (see example in the Supporting Information). Hence, a semi-infinite TL with CPE-type parameterization that describes a current decay over distance is not able to describe a short and wide pore. A more reasonable parameterization for uniform and homogenous pores may be given by constant resistances and capacitances of

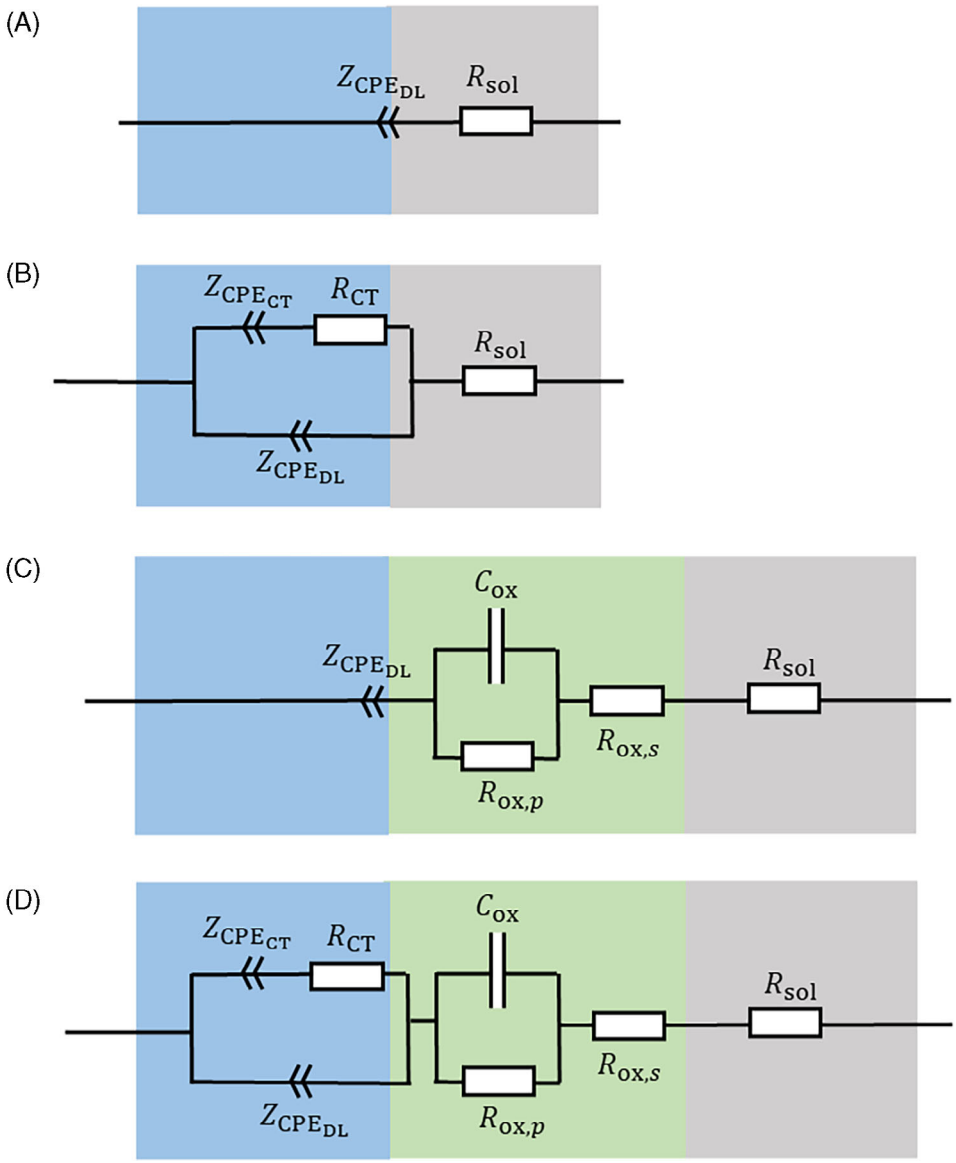

FIGURE 2 | Equivalent circuit models (ECMs) for the electrochemical interface excluding the electrolyte resistance, so that they can be directly inserted as Z^k into the generalized transmission line of Figure 1F. Blueish shaded areas: electrolytic phase. Greenish shaded areas: oxide layer. Greyish shaded area: Bulk of the electrode. (A) ECM for the double layer. (B) ECM for the double layer in combination with a charge transfer reaction. This circuit plus a series resistance is in this study denoted as 'modified Randles circuit'. (C) ECM for the double layer of an oxide-covered electrode without a charge transfer reaction. (D) ECM for the double layer of an oxide-covered electrode in combination with a charge transfer reaction.

the ladder steps of finite TLs (see results on the carbon fleece electrode). In the Supporting Information, the effect of resistive damping on capacitive currents is discussed for a straight-wall pore as a thought experiment.

3 | Results and Discussion

First, an overview of the considered electrodes is given, and the selections of ECMs are motivated. Second, the measured EIS and CV data from the first part of this study are simulated. Hereto, physicochemical assumptions to parameterize the ECMs are discussed. An automized parameter regression such as the typically used 'method of least squares' to fit the parameters of the ECMs to the measured data is intentionally avoided due to the parameter ambiguity. The parameterization accuracies and reliabilities are critically discussed for each of the presented electrodes. Third, the gained understanding to parameterize the discussed electrodes is discussed from a more generalized perspective.

3.1 | Overview of Electrodes and ECM Selection

The first part of this study showed EIS and CV data of a variety of different electrodes, from which five will be considered in more detail in the following, each representing a different morphology or electrochemical interface in terms of oxide coverage or charge transfer reactions. This section provides an overview of these electrodes and the ECMs used for the simulation of their CV and EIS responses.

The EIS response of the polished gold electrode in nitrogen-purged perchloric acid electrolyte was precisely described by a serial connection of an electrolyte resistance and a CPE (see Figure 1A) in the first part of this study. However, this circuit (in the following denoted as CPE-ECM) was not able to represent the response of the electrode in oxygen-purged perchloric acid electrolyte, especially at frequencies below 1 kHz, as it does not include the charge transfer of the electrochemical oxygen reduction reaction. This electrode is here simulated with the electrochemical interface of Figure 2B in combination with the electrolyte resistance. This ECM is denoted as 'modified Randles circuit', displaying a modification of the original Randles circuit [52, 53] (parallel combination of capacitance for the DL and resistance for the charge transfer united a series resistance for the electrolyte) by accounting for the CPE-type characteristics of the DL and diffusion-limited charge transfer process, respectively.

The glassy carbon electrode did not show significant oxygen reduction activity at 0.5 V versus RHE in perchloric acid electrolyte. Hence, it represents an inert electrode that is described by the electrochemical interface shown in Figure 2A. The EIS and CV responses of the carbon electrodes showed features that were associated with conductivity-limited microstructures. The Type 1 glassy carbon electrode (denoted as 'Type 1 GC') consists of a polished surface, which is interrupted by cracks and pores (see Supporting Information of the first part). The ECM in Figure 1E represents this case, with a distinct parameterization for the plane contributions of the surface and a CTL for the cracks and pores. Moreover, glassy carbon is known to have a porous structure [54], which might lead to electrolyte uptake and contributions to the CTL. The response of the graphite plate of the first part represents a similar system as the Type 1 GC specimen, and its capacitance dispersion is shown in the graphical abstract to this article. As its evaluation procedure is like that of the GC plate, the results are shown in the Supporting Information.

The four stacked Freudenberg E35 carbon fleeces in 100 mM perchloric acid (in the following, defined as 'carbon fleeces') represent another electrode without significant contributions of charge transfer reactions. Unlike the Type 1 GC electrode, the pores are wide and homogenous, while the contributions of its plane part to the DL response are expected to not distinctly vary from that inside the pores. Hence, without distinguishing between the plane contribution and that of the pores, the ECM of Figure 1D is used to simulate the response.

In the first part, EIS data on a titanium, ruthenium, platinum and nickel electrode were presented under a stepwise potential increase ramp, showing that the formation of oxide layers drastically impacts the DL response. The ruthenium electrode shows metal-like electronic conductivity of its oxide [55]. Ruthenium also displays a catalyst for the oxygen reduction reaction, for which the modified Randles circuit is used to account for the reduction of oxygen impurities in the electrolyte. The electrochemically formed hydrous oxide on ruthenium shows a complex microstructure with an unknown phase composition of metallic ruthenium, oxidized ruthenium, and water intercalation [56, 57]. The water intercalation can be understood as a kind of nano-porosity with ionic conductivity. This eventual nano-porosity and associated conductivity restrictions are not included in the ECM and display a source of error.

The titanium electrode represents a model system for a microstructured oxide layer for the following reasons: (i) Once titanium-oxide is formed, it cannot be reduced to metallic titanium in the considered potential range between 0.1 and 1.5 V versus RHE. (ii) The oxide layer is porous and penetrable by the electrolyte [58]. (iii) The oxidized titanium surface is expected as semi-conducting [59, 60], which leads to conductivity-limiting structures. (iv) The porosity enables a continuous electrochemical growth of the oxide layer [61] (see bypass currents in the Supporting Information of the first part). These different effects are included in the electrochemical interface of Figure 2D in combination with the generalized TL of Figure 1F that accounts for the porous oxide layer. However, based on the experimetnal data such complex ECMs are just ambiguously parameterizable. Alternatively, the electrochemical interface of Figure 2C in combination of an electrolyte resistance will be used to model the measured responses of the titanium electrode, neglecting the contributions coming from the porous microstructure.

In the case of the platinum electrode, pseudocapacitances [36] and surface redox reactions complicate the interpretation of the EIS data. In the case of nickel electrode, the phase changes between nickel hydroxide and oxyhydroxide in combination with hydrous structures further increase the difficulties in interpreting the EIS and CV data from the first part [62, 63]. The measured responses of the platinum and nickel electrode are not analyzed with ECMs here, as their parameterizations are in the opinion of the authors' speculation due to the number of different physicochemical effects contributing and the resulting overwhelming complexity.

3.2 | The Polished Gold Electrode

Figure 3 shows the measured and simulated EIS and CV response of the gold electrode in oxygen-purged perchloric acid electrolyte. The simple ECM of the electrolyte resistance in combination with a CPE (defined as CPE-ECM) shown in Figure 1A serves as a reference and is compared to the above-discussed modified Randles circuit (ECM of Figure 2B in combination with a resistor for the electrolyte). For both ECMs, the electrolyte resistance and the CPE for the DL are parameterized with the fit discussed in the first part of this study ($R_{liq} = 1.6\ \Omega$, $n_{DL} = 0.92$, $\xi_{DL} = 107{,}448\ \Omega\ \mathrm{Hz}^n$). The CPE and a resistor for the diffusion-limited oxygen reduction are parameterized with $R_{CT} = 50{,}000\ \Omega$, $\xi_{CT} = 24{,}000\ \Omega\ \mathrm{Hz}^n$, and $n_{CT} = 0.3$.

Above 50 Hz, the CPE-ECM and the modified Randles circuit show equal simulated EIS data as the contribution of the oxygen reduction reaction negligibly affects the response. Below 50 Hz, the measured phase angle and the values in the capacitance dispersion increase because of the oxygen reduction. In Figure 3D, the simulated CV data (ranging from 0.1 to 1 Hz) with the CPE-ECM also show deviations from the measured data. With modified Randles (Figure 3E), the magnitudes and slopes of the measured CV data are adequately represented, although the measurements are affected by a significant offset due to the oxygen reduction current which is absent in the simulated response. The bypass current discussed in the first part of this study is responsible for this offset, which is not directly measured with EIS. Consequently, this information is missed when the CV

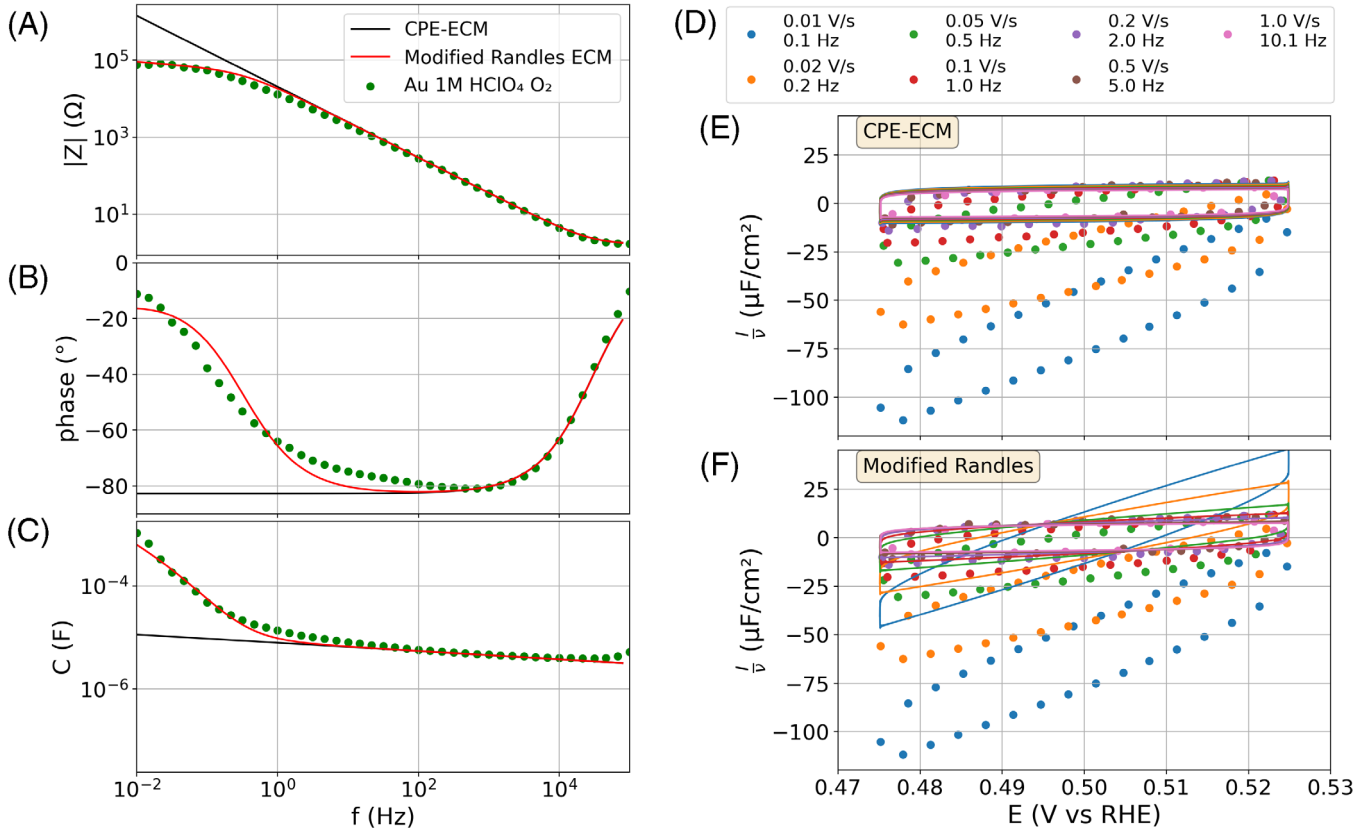

FIGURE 3 | Measured (dots) and simulated (lines) data on the polished gold electrode with a constant phase element (CPE)-based model and the modified Randles circuit (electrochemical interface of Figure 2B in combination with an electrolyte resistance). (A) Impedance magnitude. (B) Impedance phase angle. (C) Capacitance dispersion extracted from the impedance data. (D) Legend for the CV data with scan rate and frequency. (E) CV data at an amplitude of 50 mV. Simulations using the CPE-ECM. (F) CV data at an amplitude of 50 mV. Simulations with the modified Randles circuit.

data are simulated based on the EIS data. Subsequent subtraction of the bypass current to the CV data could correct this offset, which is here not conducted to explicitly show its effect on the response.

The modified Randles circuit consists of seven parameters in total: three resistances (R_{liq}, R_{sol} and R_{CT}) and two CPEs ($Z_{CPE_{DL}}$ and $Z_{CPE_{CT}}$) that are characterized by four parameters (n_{DL}, ξ_{DL}, n_{CT}, ξ_{CT}). With the nitrogen-purged electrolyte, the CPE for the DL and the serial resistance (R_s, n_{DL} and ξ_{DL}) can be reliably determined to the above-mentioned values as discussed in the first part of this study. In addition, the resistance of the solid phase R_{sol} can be assumed as negligible due to the good conductivity of the gold specimen, so that the electrolyte resistance equals the serial resistance: $R_{liq} = R_s$. Hence, three parameters of the charge transfer reaction (R_{CT}, n_{CT} and ξ_{CT}) remain. However, these three parameters are ambiguous, as several combinations can lead to good matching fits to the EIS data.

3.3 | The Glassy Carbon Electrode

In the first part, the surface cracks and holes of the glassy carbon electrodes were discussed to lead to resistive damping of capacitive currents. The simulated responses shall be independent of the lengths of ladder networks (see Supporting Information for detailed results on the variation of the ladder lengths); otherwise, the ladder length itself acts as an additional parameter with arbitrary values. In the first part of this study, the CPE-ECM was shown to precisely describe the measured impedance spectra above 50 Hz for the Type 1 GC electrode. At these frequencies, the pores negligibly contribute to the response due to the resistive damping of capacitive currents. The fit parameters of the CPE-ECM from the first part are identified with the elements that describe the plane part of the electrode ($R_{liq} + R^p_{sol}$, Z^p_{CPE}). The electric resistance in the solid phase is assumed as negligible due to the good conductivity of the electrode. Thus, the resistances R^p_{sol} and R^k_{sol} are identified with zero.

The cracks and holes of the Type 1 GC electrode are characterized by using the following assumptions: (i) The pores and cracks are tapered. This effect is estimated to linearly increase of the resistances R^k_{liq} along the ladder as the cross section decreases by the narrowing towards the apex (end of the pore). (ii) In the tapered pores, the pore perimeter decreases towards the apex. Consequently, the surface area in the segments of the ladder network decreases towards the apex. Based on a linear relation of surface area and capacitance, the CPE-prefactors ξ^k are reciprocally proportional to the surface area. As a rough estimation, the values of ξ^k are assumed to correlate linearly with the ladder step. (iii) The exponent of Z^k_{CPE} is assumed as independent of the pore intrusion and the ladder step k; however,

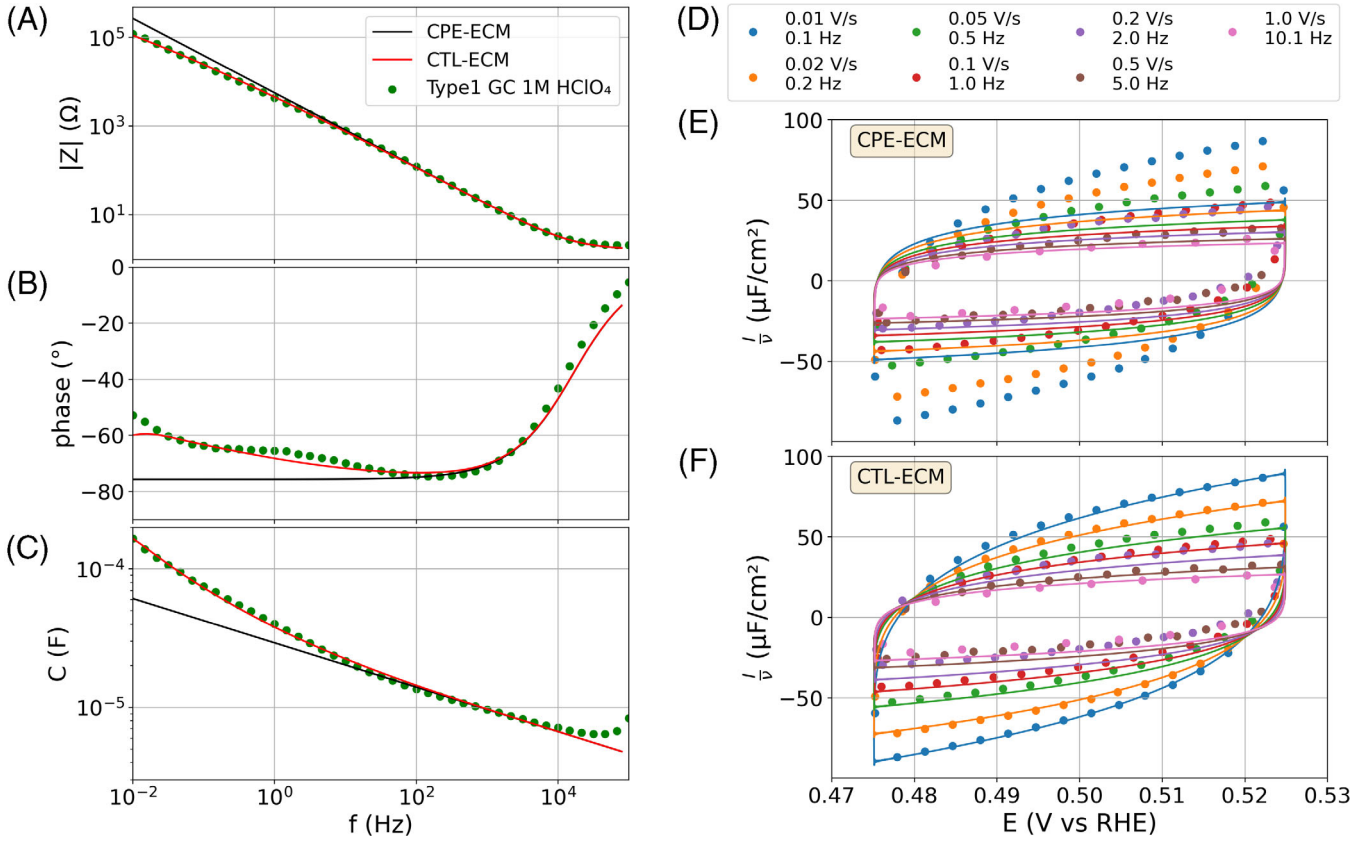

FIGURE 4 | Measured (dots) and simulated (lines) data on the Type 1 GC electrode with a constant phase element (CPE)-based ECM and convoluted transmission line (CTL) ECM. (A) Impedance magnitude. (B) Impedance phase angle. (C) Capacitance dispersion extracted from the impedance data. (D) Legend for the CV data with scan rate and frequency. (E) CV data at an amplitude of 50 mV. Simulations with the CPE-ECM. (F) CV data at an amplitude of 50 mV. Simulations with the CTL-ECM.

the detailed physicochemical effects of the pore size on the values of the exponent are unknown. With these assumptions, the resistances and CPE-prefactors of the CTL were calculated as

$$R_{\text{liq}}^{k} = 1000 \cdot (1 + k)\ \Omega \tag{9}$$

and

$$\xi^{k} = 4 \cdot 10^{5} + 400 \cdot (1 + k)\ \Omega\ \text{Hz}^{n}. \tag{10}$$

The absolute values for offsets ($R_{\text{liq}}^{0} = 1000\ \Omega$ and $\xi^{0} = 40,400\ \Omega\ \text{Hz}^{n}$) and slopes of the linear interpolation (1000 Ω for the resistances and 400 Ω Hz^{n} for the CPE-prefactors) were manually adjusted so that the simulated impedance data fit to the measured response.

Figure 4 shows the simulated and measured responses of the GC Type 1 electrode, where the CPE-ECM serves as a reference. Below 100 Hz, the CPE-ECM simulation shows significant deviations from the measured impedance, which have been attributed to the influence of cracks and holes in the first part of this study. With the CTL-ECM, a good agreement between measured and simulated data is achieved. Like the impedance data, the CV data simulated with the CPE-ECM show distinct deviations from the measured data (see Figure 4D). However, with the CTL-ECM approach, the simulated and measured CV match reasonably well. The capacitive contributions of the pores increasingly contribute towards low frequencies as more parts of the tapered pores turn from a resistively dominated regime into a capacitively dominated regime (with respect to the individual relaxation frequencies of the CTL steps) where they significantly contribute to the response.

Every crack or hole of the Type 1 GC is different, whereas the ECM was parameterized with the assumption of equally linear tapered pores. This assumption may represent an average of the response, in which the superposition of all cracks and holes smooths individual features. However, this approach is not a physicochemically correct parameterization of the microstructure. Every combination of CPEs and resistances with similar resistive to capacitive ratios will be able to lead to similar simulated responses, so that the parameterization is ambiguous. As a result, the interpretation of pore widths or depths based on the EIS and CV data is speculative. With a well-known topology of the surface, an impedance network model may be able to generate an adequate ECM to simulate the EIS and CV data. However, based on these EIS or CV data, the topology cannot be reconstructed.

3.4 | The Carbon Fleece Electrodes

Figure 5 shows the simulated impedance and CV responses of the carbon fleeces in comparison to the measured data. The

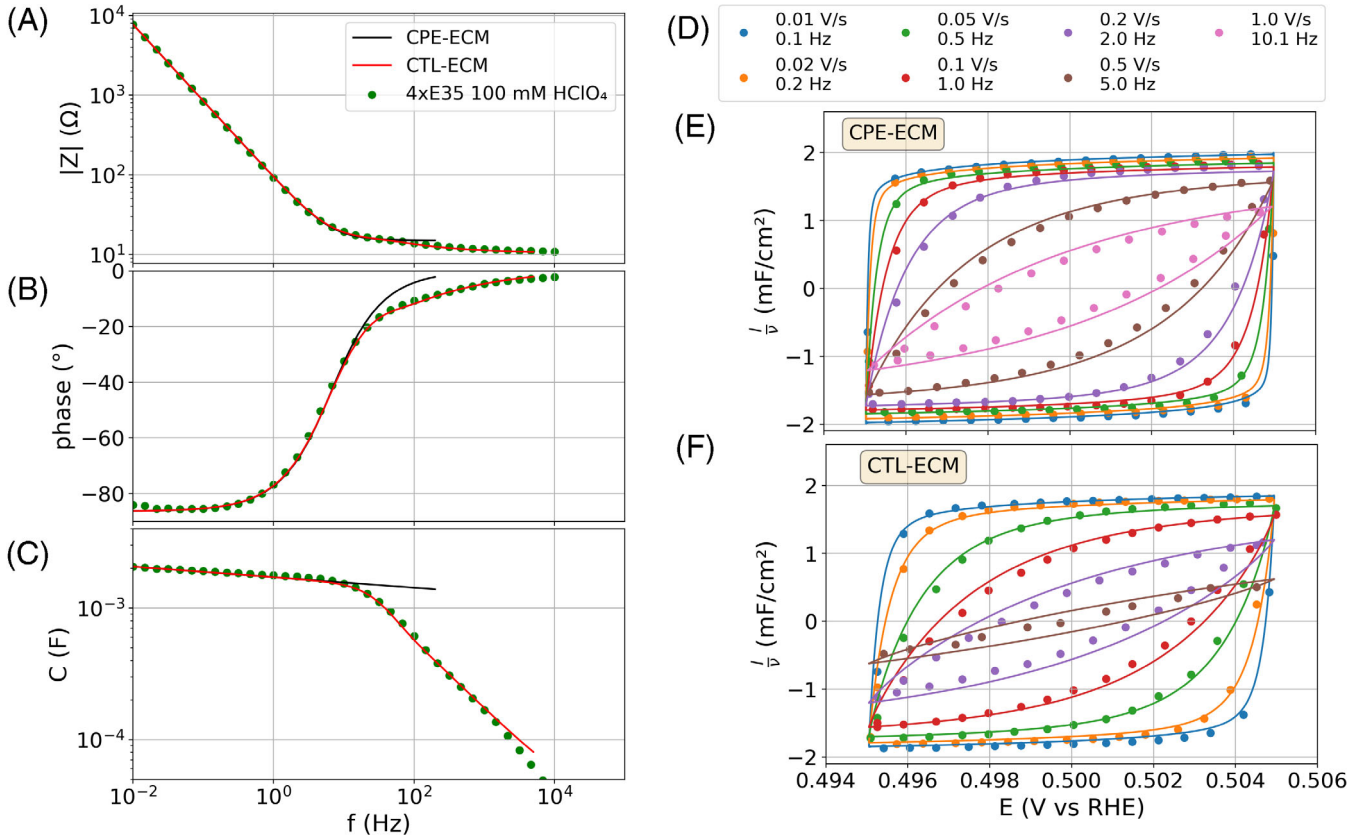

FIGURE 5 | Measured (scatter) and simulated (lines) data on the four stacked E35 carbon fleeces in 100 mM perchloric acid with a CPE-ECM and a CTL-ECM. (A) Impedance magnitude. (B) Impedance phase angle. (C) Capacitance dispersion extracted from the impedance data. (D) Legend for the CV data with scan rate and frequency. (E) CV data at an amplitude of 50 mV. Simulations with the CPE-ECM. (F) CV data at an amplitude of 50 mV. Simulations with the CTL-ECM.

parameters of the CTL-ECM (Figure 1D) that represent the carbon fleeces were determined based on the following observations of the measured EIS data: (i) The electrical resistance of the sheets is negligible, for which $R^k_{\text{sol}} = 0$. (ii) The lowest measured resistance of 10 Ω of the electrode (see Figure 5A) is identified with the serial resistance at $k = 0$ of the ECM, which equals $R_{\text{liq}} + R^0_{\text{liq}}$. (iii) Based on this measured response, the resistances of the ladder steps are parameterized by

$$R^k_{\text{liq}} = \frac{15}{\text{L}}\ \Omega, \tag{11}$$

which is found to adequately represent the measured frequency dependency of the impedance above 200 Hz. (iv) The capacitive contributions to the impedance are assumed as equal along the ladder network due to a homogenous pore size distribution. Hence, the values of n^k and ξ^k of Z^k_{CPE} are assumed as independent of the ladder step k. In the case of negligible resistive damping of the current in the pore, the equal capacitive contributions of all ladder steps shall be added. This additive behaviour of the parallel capacitances along the pore is achieved when the total CPE-prefactor ξ_{total} equals the inverse sum of the ladder steps ξ^k:

$$\xi_{\text{total}} = \left(\sum_{k=0}^{L} \frac{1}{\xi^k}\right)^{-1}. \tag{12}$$

With the assumption of equally distributed capacitances, the prefactors of the individual ladder steps are calculated by $\xi^k = \xi_{\text{total}} \times L$.

In the first part, the relaxation frequency of the electrode was estimated to 6.5 Hz. At this frequency, all ladder steps contribute to the measured capacitance, as the CPE-ECM and the CTL-ECM show equal responses. The prefactor of the CTL-ECM was in Part 1 fitted to $\xi_{\text{fit}} = 541\ \Omega\ \text{Hz}^n$ (which is not significantly impacted by the high-frequency resistive damping above a phase angle of −20°), which can be identified with ξ_{total} of Equation (12). Towards higher frequencies than the relaxation frequency, a decay of the measured capacitance due to resistive damping of the current in the pores can be seen in Figure 5C. This decay is not represented by the CPE-ECM, whereas the CTL-ECM precisely describes the measured behaviour. Again, the resistive damping of the capacitive currents in the pores is frequency dependent. Deep-lying parts of the pores (high ladder steps in the CTL-ECM) are affected by larger resistances than those close to the surface (low ladder steps) that face the reference electrode.

The simulated CV responses with the CPE-ECM (Figure 5D) and the CTL-ECM (Figure 5E) do not show significant differences. The maximum CV frequency is 10 Hz, at which the CPE-ECM and CTL-ECM showed similar responses in the impedance data (Figure 5A–C), as the relaxation in the pores becomes only significant at higher frequencies. The higher harmonics in the

Fourier transform algorithm are in the range of the resistive damping; however, these have a small impact on the simulated CV. As a result, the CPE-ECM and CTL-ECM both adequately represent the measured CV data.

Unlike the Type 1 GC specimen, the parameterization of the carbon fleeces is considered solid by the authors. The resistances in the pores of the carbon fleeces were parameterized based on the impedance data. Knowing that the pores are homogenous, every step in the CTL must have the same resistance in the liquid phase, for which the parameters R_{liq}^{k} can be precisely determined. The CPE-prefactors determined by the fit presented in the first part of this study can be identified with the inverse sum of the CPE-prefactors of the ladder steps (Equation 12). The homogenous properties of the pores are used to equally distribute the DL contributions along the ladder steps of the CTL. The ladder length variation in the Supporting Information shows that with $L \geq 30$, the ladder length has a negligible influence on the simulated response. A ladder length variation can lead to an infinite number of parameter sets that will be able to reproduce the simulated responses; however, the parameterization follows a clear portrayal of the physicochemical structure that is based on easily derivable assumptions. Nevertheless, it is not possible to supply a reconstruction of the pore geometry as an infinite number of structures can lead to similar responses.

3.5 | The Ruthenium Electrode

Figure 6 shows the EIS data of the ruthenium electrode for potentials of 0.1, 0.7 and 1.3 V versus RHE during the first stepwise potential increase ramp (see definition in the first part). The parameters for the modified Randles circuit used to simulate the measured responses are listed in Table 1. At 0.1 V, the polished ruthenium electrode shows significant contributions of the reduction of oxygen impurities from the electrolyte. Like the gold electrode, the phase angle and capacitance are increased towards lower frequencies due to the oxygen reduction reaction. At 0.7 V, the EIS data do not show significant charge transfer contributions, for which the data can be precisely described by the CPE-ECM (equal to an infite charge transfer resistance). At 1.3 V, the phase angle increases below 1 Hz.

At 1.3 V, the bypass current of the ruthenium electrode is approximately 3 μA (see Supporting Information section of the first part). This charge transfer process can be associated with a combination of a growing oxide layer, the oxygen evolution reaction or the dissolution of the ruthenium electrode [64]. The increase of the phase angle below 1 Hz may be attributable to such charge transfer processes or conductivity-limiting microstructures of the electrochemically formed oxide. Ohmic drops of the ion conduction in the nano-porosity of the hydrous oxide or the electrical conductivity of the hydrous oxide itself may significantly affect the response. Hence, the chosen ECM and its parameterization are with the state of the information not reliable for the EIS data at 1.3 V versus RHE. At this potential, the authors cannot unambiguously attribute the increase of the capacitance and phase angle towards lower frequencies to charge transfer processes or resistively damped capacitive currents in the microstructure.

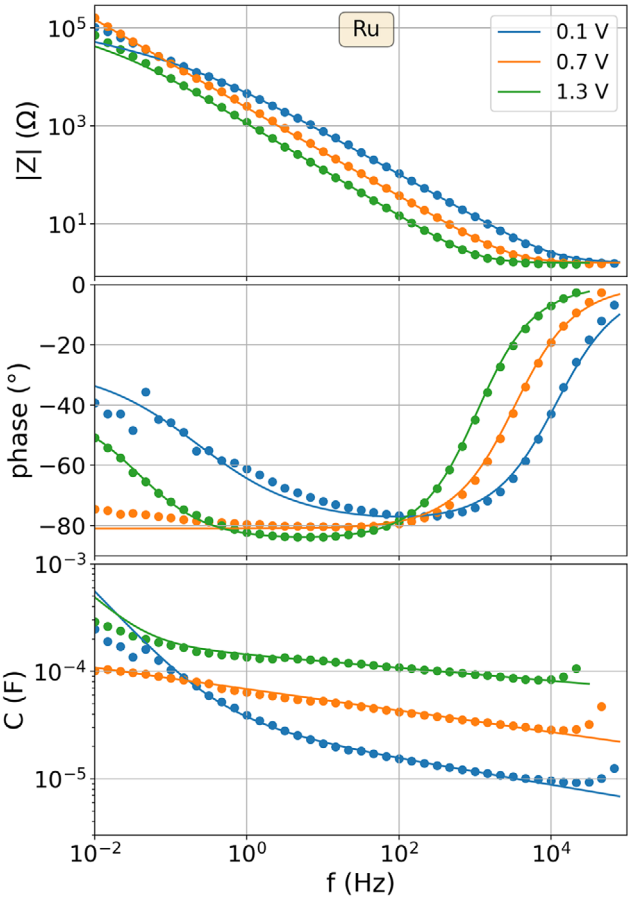

FIGURE 6 | Measured (dots) and simulated (lines) EIS data (impedance magnitude, phase angle, and capacitance dispersion) of the titanium electrode at a potential of 0.1, 0.7 and 1.3 V of the first potential increase ramp (see first part). The modified Randles circuit (electrochemical interface of Figure 2B in combination with an electrolyte resistance) was used to simulate the EIS data.

3.6 | The Titanium Electrode

Figure 7 shows the simulated and measured impedance data of the titanium electrode at potentials of 0.1, 0.7 and 1.4 V. The shown data were recorded during the first potential increase ramp (see first part). The simulation of the EIS data was conducted using the ECM of Figure 2C in combination with an additional electrolyte resistance R_{liq}. Table 2 summarizes the parameters used for this ECM. Following assumptions were used for this parameterization: (i) The electrolyte resistance R_{liq} is independent of the oxidation state. (ii) The resistance of the metallic titanium substrate is negligible. (iii) The serial resistance of the oxide $R_{\text{ox,s}}$ was assumed as negligible. (iv) The parallel resistance of the oxide $R_{\text{ox,p}}$ was assumed to increase with a growing oxidation layer. (v) The CPE-prefactor ξ was assumed to decrease with a growing oxidation layer, representing an increase of the capacitance by an increase of the wetted surface area in the porous oxide layer. (vi) The CPE-exponent n is assumed as independent of the oxidation state. (vi) A growing oxide layer decreases the capacitance of C_{ox}, like the capacitance of a plate capacitor that increases with larger distances between the plates.

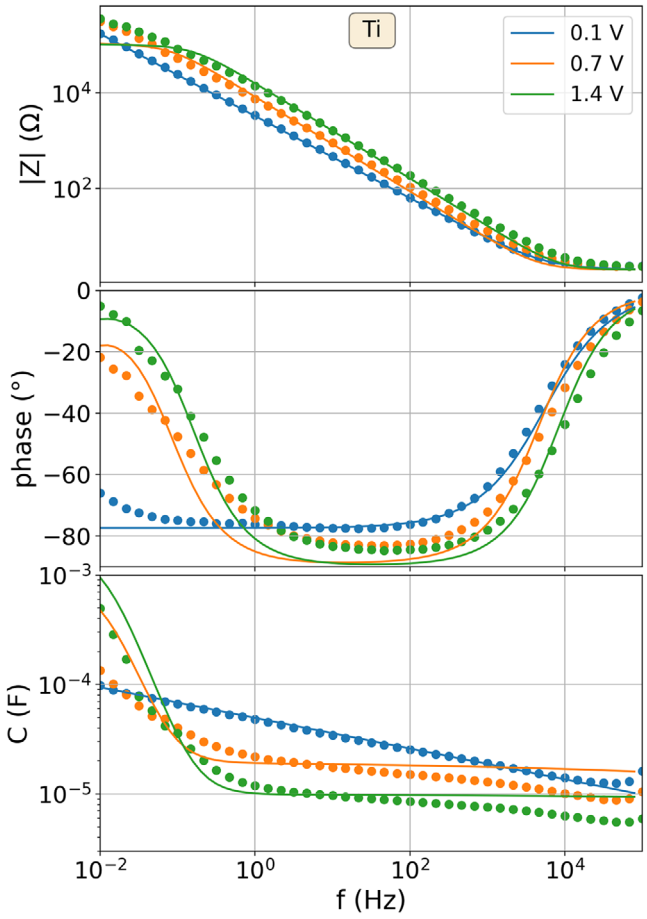

FIGURE 7 | Measured (dots) and simulated (lines) EIS data (impedance magnitude, phase angle, and capacitance dispersion) of the titanium electrode at a potential of 0.1, 0.7 and 1.4 V of the first potential increase ramp (see first part). The electrochemical interface of Figure 2C in combination with an electrolyte resistance was used to simulate the EIS data.

Using this ECM, the following physicochemical effects were neglected: (i) the porosity of the formed oxide layer and any gradients of such, (ii) changes in the conductivity and wetted surface areas within this oxide, (iii) any charge transfer reactions that are associated with the continuous growth of the oxide layer on the titanium electrode, (iv) any gradients in the composition of titanium and titanium dioxide and (v) electronic band structure intrusion among the titanium-metal phase, the titanium-oxide phase, and the electrolyte. Maybe even more effects may contribute to the measured response that the authors are not aware of. However, even with the employed simplified circuit, the experimental data can be reasonably represented. Hence, the ambiguity of the parameters is, in the opinion of the authors, too large to draw any conclusions about the detailed microstructure or physicochemical processes at the titanium electrode based on the presented EIS data.

3.7 | Discussion on the Parameterization Ambiguity

Above sets of parameters that describe the DL responses of five different electrodes were presented, each representing a different electrochemical interface or microstructure. The aim of the following discussion is to derive generalized conclusions from the discussed case studies. The more elements an ECM contains, the more ambiguous its parameterization becomes. Hence, simple ECMs are favourable for unambiguous parameterizations. However, the elements of an ECM should represent all the physicochemical mechanisms that contribute to the electrochemical response of an electrode. Resistively damped capacitive currents in microstructures require the complexity of CTLs to portray the resistive–capacitive interplay in the pores, which comes at the price of many parameters. With a well-known microstructure (such as in the case of the carbon fleece), physicochemical assumptions may be made that allow reasonable parameterizations. However, other sets of parameters will always allow to simulate similar responses. This ambiguous parameterization means that pore

TABLE 1 | Parameters for the modified Randles circuit (Figure 2B plus R_{liq} to parameterize the ionic resistance) used in Figure 6 to model the electrochemical impedance spectroscopy data for the different potentials E on the ruthenium electrode.

E (V)	R_{liq} (Ω)	R_{sol} (Ω)	ξ_{DL}	n_{DL}	R_{CT} (Ω)	ξ_{CT}	n_{CT}
0.1	1.6	0	30,705	0.88	30	25,000	0.3
0.7	1.6	0	12,308	0.9	10^{10}	1	1
1.3	1.6	0	6326	0.94	10,000	10,000	0.5

Note: In the case of the equivalent circuit model for the 0.7 V data, a charge transfer resistance of 10^{10} Ω displays a chemically inert electrode. This high resistance values makesd the values of ξ_{CT} and n_{CT} meaningless.

TABLE 2 | Parameters for the equivalent circuit model (Figure 2C plus R_{liq} to parameterize the ionic resistance) used in Figure 7 to model the electrochemical impedance spectroscopy data for the different potentials E.

E (V)	R_{liq} (Ω)	R_{sol} (Ω)	$R_{ox,s}$ (Ω)	$R_{ox,p}$ (Ω)	ξ	n	C_{ox} (F)
0.1	2	0	0	0.01	1.6×10^4	0.86	10^{-2}
0.7	2	0	0	10^5	2×10^3	0.86	2×10^{-5}
1.4	2	0	0	10^5	1×10^3	0.86	10^{-5}

structures cannot be reconstructed based on measured EIS and CV responses.

Even with inert electrodes such as the Type 1 GC electrode, it is not possible to reasonably estimate the microstructure based on EIS or CV data, as various pore geometries can lead to similar resistively damped capacitive currents. The EIS and CV data display superpositions of spatially distributed contributions of the different elements in the ECMs. This superposition leads to an information loss about the location of the elements. As a result, an unlimited number of parameter combinations will lead to reasonable fits to the experimental data. Hence, with respect to the varying pore geometries of the Type 1 GC electrode, it is not possible to make reasonable assumptions for the parametrization with the one-dimensional ECMs presented in Figure 1. Three-dimensional ECM describing the entire specimen topology may be able to simulate the EIS data correctly, yet, these have to be supplied by topography data.

For most oxide-covered electrodes with porous microstructures such as the titanium electrode, a superposition of many physicochemical effects contributes to the measured response. The individual contributions of these different effects are often not distinguishable, which is, for example, discussed for the similarity of the contributions of charge transfer processes and resistively damped capacitive currents in microstructures to the EIS data. The complexity of oxide-covered electrodes requires ECMs with overwhelming numbers of parameters. For such systems, reasonable quantitative information on the electrochemical interface or the microstructure based on measured EIS or CV approaches seem impossible. Hence, the authors point out that EIS and CV data of most oxide electrodes are prone to misinterpretation due to the pitfall of ambiguous parameterization possibilities. Ruthenium and iridium may display an outstanding example due to the metallic conductivities of their oxides [55]. However, even in this case, the authors of this study are unsure about the reliability of the employed ECM and its parameterization.

4 | Conclusions

In this study, ECMs to describe microstructures, oxide layers and charge transfer reactions were developed and parameterized. These ECMs were used to simulate the measured EIS and CV data of five selected electrodes from the first part of this study. The TL model for pores was further developed by combining previously reported approaches into a CTL-ECM. The complexity described by the CTL-ECM was discussed as necessary to describe the DL response of microstructures with resistively damped capacitive currents. The impedances of such CTL-ECMs were calculated in a newly developed mixed analytical–numerical computational framework (source codes provided in the Supporting Information). With these CTL-ECMs, the simulated EIS and CV data can resemble the measured data of the porous carbon electrodes; however, the parameterization is, in most cases, ambiguous. Microstructures cannot be reconstructed based on the measured data as an infinite number of structures can lead to similar responses. Local contributions are blended in the response that finally leads to a loss of information in the EIS or CV data. Moreover, ECMs to describe oxidized electrodes with semi-conducting and micro-porous oxide coverage as well as charge transfer reactions were discussed and compared to the experimental results. For such electrodes, the overwhelming complexity of ECMs to describe all occurring physicochemical effects leads to many parameters that cannot be unambiguously fitted. To summarize, with the presented case studies limitations and pitfalls of the physicochemical interpretation of EIS and CV data with ECMs are elucidated.

Nomenclature

C^k	capacitance of the kth step of the transmission line
C_{ox}	capacitance value of C_{EIS} at a phase angle of 45° during the resistive-capacitive relaxation
E	electrode potential
f	frequency
i	complex number
k	ladder step of the transmission line
n^k	exponent of the CPE of the kth step of the transmission line
n_{CT}	exponent of the CPE of a charge transfer reaction
n_{DL}	exponent of the CPE of the double layer capacitance
n_{fit}	exponent of the CPE determined by a fit to an impedance spectrum
phase	phase angle of the impedance
R_{CT}	charge transfer reaction
R_{liq}	electrolyte resistance between the reference electrode and the surface of the working electrode
R^k_{liq}	electrolyte resistance of the kth step of the transmission line
$R_{ox,p}$	parallel electric resistance of a leaky oxide capacitor
$R_{ox,s}$	serial electric resistance of an oxide layer
R_s	serial resistance of the equivalent circuit
$R_{s,fit}$	serial resistance determined by a fit to an impedance spectrum
R_{sol}	resistance of the solid phase of the electrode
R^k_{sol}	electric resistance in the solid phase of the kth step of the transmission line with reference to the alignment in Figure 2D
$\tilde{R}^k_{sol}$	electric resistance in the solid phase of the kth step of the transmission line with reference to the alignment in Figure 2D
R^p_{sol}	electric resistance in the solid phase attributable to the contributions of the plane component
$\|Z\|$	impedance magnitude
Z_{1F}	impedance of Figure 1F
Z_{2A}	impedance of Figure 2A
Z_{2B}	impedance of Figure 2B
Z_{2C}	impedance of Figure 2C
Z_{2D}	impedance of Figure 2D
Z^k	impedance of the part of the impedance
Z^p	impedance attributable to the contributions of the plane component

Z_{CPE}	impedance of a CPE
Z_{CPE}^{k}	impedance of the CPE of the kth step of the transmission line
Z_{CPE}^{p}	impedance of the CPE attributable to the contributions of the plane component
$Z_{CPE_{CT}}$	impedance of the CPE related to the charge transfer
$Z_{CPE_{DL}}$	impedance of the CPE related to the DL
π	pi
ξ^{k}	prefactor CPE of the kth step of the transmission line
ξ_{CT}	prefactor CPE for the diffusion limitation of a charge transfer reaction
ξ_{DL}	prefactor CPE of the double layer
ξ_{fit}	prefactor CPE determined by a fit to an impedance spectrum

Acknowledgements

This work was supported by the German Federal Ministry of Education and Research (BMBF) within the Project PhasKat (033RC028E).

Conflicts of Interest

The authors declare no conflicts of interest.

Data Availability Statement

The codes used for the data evaluation are all accessible in the Supporting Information of this article. All raw data are plotted. Data available on request from the authors.

References

1. H. Helmholtz, "Studien über electrische Grenzschichten," *Annalen der Physik und Chemie* 243, no. 7 (1879): 337–382.

2. M. Gouy, "Sur la constitution de la charge électrique à la surface d'un électrolyte," *Journal de Physique Théorique et Appliquée* 9 (1910): 457–468.

3. D. L. Chapman, "A Contribution to the Theory of Electrocapillarity," *The London, Edinburgh, and Dublin Philosophical Magazine and Journal of Science* 25 (1913): 475–481.

4. O. Stern, "Zur theorie der elektrolytischen doppelschicht," *Zeitschrift für Elektrochemie und Angewandte Physikalische Chemie* 30 (1924): 508–516.

5. D. C. Grahame, "Properties of the Electrical Double Layer at a Mercury Surface. I. Methods of Measurement and Interpretation of Results," *Journal of the American Chemical Society* 63 (1941): 1207–1215.

6. D. C. Grahame, "Properties of the Electrical Double Layer at a Mercury Surface. II. The Effect of Frequency on the Capacity and Resistance of Ideal Polarized Electrodes," *Journal of the American Chemical Society* 68 (1946): 301–310.

7. M. Schalenbach, V. Selmert, A. Kretzschmar, et al., "How Microstructures, Oxide Layers, and Charge Transfer Reactions Influence Double Layer Capacitances. Part 1: Impedance Spectroscopy and Cyclic Voltammetry to Estimate Electrochemically Active Surface Areas (ECSAs)," *Physical Chemistry Chemical Physics* 26 (2024): 14288–14304.

8. G. J. Brug, A. L. G. van den Eeden, M. Sluyters-Rehbach, and J. H. Sluyters, "The Analysis of Electrode Impedances Complicated by the Presence of a Constant Phase Element," *Journal of Electroanalytical Chemistry* 176 (1984): 275–295.

9. W. R. Fawcett, Z. Kováčová, A. J. Motheo, and C. A. Foss, "Application of the AC Admittance Technique to Double-Layer Studies on Polycrystalline Gold Electrodes," *Journal of Electroanalytical Chemistry* 326 (1992): 91–103.

10. A. J. Motheo, J. R. Santos, A. Sadkowski, and A. Hamelin, "The Gold (210)/Perchloric Acid Interface: Impedance Spectroscopy," *Journal of Electroanalytical Chemistry* 397 (1995): 331–334.

11. A. J. Motheo, A. Sadkowski, and R. S. Neves, "Electrochemical Immittance Spectroscopy Applied to the Study of the Single Crystal Gold/Aqueous Perchloric Acid Interface," *Journal of Electroanalytical Chemistry* 430 (1997): 253–262.

12. T. Pajkossy, "Capacitance Dispersion on Solid Electrodes: Anion Adsorption Studies on Gold Single Crystal Electrodes," *Solid State Ionics* 94 (1997): 123–129.

13. T. Pajkossy, "Impedance Spectroscopy at Interfaces of Metals and Aqueous Solutions—Surface Roughness, CPE and Related Issues," *Solid State Ionics* 176 (2005): 1997–2003.

14. P. Zoltowski, "On the Electrical Capacitance of Interfaces Exhibiting Constant Phase Element Behaviour," *Electroanalytical Chemistry* 443 (1998): 149–154.

15. M. Schalenbach, Y. E. Durmus, S. Robinson, H. Tempel, H. Kungl, and R. Eichel, "The Physicochemical Mechanisms of the Double Layer Capacitance Dispersion and Dynamics: An Impedance Analysis," *The Journal of Physical Chemistry C* 125 (2021): 5870–5879.

16. J. Huang, Y. Gao, J. Luo, et al., "Impedance Response of Porous Electrodes: Theoretical Framework, Physical Models and Applications," *Journal of the Electrochemical Society* 167 (2020): 166503.

17. R. De Levie, "On Porous Electrodes in Electrolyte Solutions-IV," *Electrochimica Acta* 9 (1964): 1231–1245.

18. O. E. Barcia, E. D'Elia, I. Frateur, O. R. Mattos, N. Pébère, and B. Tribollet, "Application of the Impedance Model of de Levie for the Characterization of Porous Electrodes," *Electrochimica Acta* 47 (2002): 2109–2116.

19. M. Itagaki, Y. Hatada, I. Shitanda, and K. Watanabe, "Complex Impedance Spectra of Porous Electrode With Fractal Structure," *Electrochimica Acta* 55 (2010): 6255–6262.

20. S. J. Lenhart, D. D. Macdonald, and B. G. Pound, "An AC Impedance Study of the Degradation of Porous Nickel Battery Electrodes," *Journal of the Electrochemical Society* 135 (1988): 1063–1071.

21. W. J. Albery and A. R. Mount, "Application of a Transmission Line Model to Impedance Studies on a Poly(vinylferrocene)-Modified Electrode," *Journal of the Chemical Society Faraday Transactions* 89 (1993): 327–331.

22. F. Hilario, V. Roche, A. M. Jorge, and R. P. Nogueira, "Application of the Transmission Line Model for Porous Electrodes to Analyse the Impedance Response of TiO2 Nanotubes in Physiological Environment," *Electrochimica Acta* 253 (2017): 599–608.

23. J. Hong, A. Bhardwaj, Y. Namgung, H. Bae, and S. J. Song, "Evaluation of the Effects of Nanocatalyst Infiltration on the SOFC Performance and Electrode Reaction Kinetics Using the Transmission Line Model," *Journal of Materials Chemistry A* 8 (2020): 23473–23487.

24. F. La Mantia, J. Vetter, and P. Novák, "Impedance Spectroscopy on Porous Materials: A General Model and Application to Graphite Electrodes of Lithium-Ion Batteries," *Electrochimica Acta* 53 (2008): 4109–4121.

25. J. Costard, J. Joos, A. Schmidt, and E. Ivers-Tiffée, "Charge Transfer Parameters of $Ni_xMn_yCo_{x1—y}$ Cathodes Evaluated by a Transmission Line Modeling Approach," *Energy Technology* 9 (2021): 2000866.

26. W. J. Albery and A. R. Mount, "Dual Transmission Line With Charge-Transfer Resistance for Conducting Polymers," *Journal of the Chemical Society Faraday Transactions* 90 (1994): 1115–1119.

27. J. Bisquert, "Influence of the Boundaries in the Impedance of Porous Film Electrodes," *Physical Chemistry Chemical Physics* 2 (2000): 4185–4192.

28. Q. A. Huang, Y. Li, K. C. Tsay, et al., "Multi-Scale Impedance Model for Supercapacitor Porous Electrodes: Theoretical Prediction and Experimental Validation," *Journal of Power Sources* 400 (2018): 69–86.

29. N. Ogihara and Y. Itou, "Mathematical Model Based on Staircase Structure for Porous Electrode Impedance," *Physical Chemistry Chemical Physics* 24 (2022): 21863–21871.

30. J. Bisquert, G. Garcia-Belmonte, F. Fabregat-Santiago, N. S. Ferriols, P. Bogdanoff, and E. C. Pereira, "Doubling Exponent Models for the Analysis of Porous Film Electrodes by Impedance. Relaxation of TiO_2 Nanoporous in Aqueous Solution," *Journal of Physical Chemistry B* 104 (2000): 2287–2298.

31. H. Nara, D. Mukoyama, T. Yokoshima, T. Momma, and T. Osaka, "Impedance Analysis With Transmission Line Model for Reaction Distribution in a Pouch Type Lithium-Ion Battery by Using Micro Reference Electrode," *Journal of the Electrochemical Society* 163 (2016): A434–A441.

32. P. M. Biesheuvel, Y. Fu, and M. Z. Bazant, "Diffuse Charge and Faradaic Reactions in Porous Electrodes," *Physical Review E* 83 (2011): 061507 .

33. P. M. Biesheuvel, Y. Fu, and M. Z. Bazant, "Electrochemistry and Capacitive Charging of Porous Electrodes in Asymmetric Multicomponent Electrolytes," *Russian Journal of Electrochemistry* 48 (2012): 580–592.

34. J. C. Wang, "Realizations of Generalized Warburg Impedance With RC Ladder Networks and Transmission Lines," *Journal of the Electrochemical Society* 134 (1987): 1915–1920.

35. M. Schalenbach, Y. E. Durmus, H. Tempel, H. Kungl, and R. A. Eichel, "A Dynamic Transmission Line Model to Describe the Potential Dependence of Double-Layer Capacitances in Cyclic Voltammetry," *Journal of Physical Chemistry C* 125 (2021): 27465–27471.

36. M. Schalenbach, Y. E. Durmus, H. Tempel, H. Kungl, and R. A. Eichel, "The Role of the Double Layer for the Pseudocapacitance of the Hydrogen Adsorption on Platinum," *Scientific Reports* 12 (2022): 1–10.

37. J. Huang, "Diffusion Impedance of Electroactive Materials, Electrolytic Solutions and Porous Electrodes: Warburg Impedance and Beyond," *Electrochimica Acta* 281 (2018): 170–188.

38. I. Shitanda, S. Tsujimura, H. Yanai, Y. Hoshi, and M. Itagaki, "Electrochemical Impedance Simulation of Branch Structure Porous Carbon Electrode Using Transmission Line Model," *Electrochemistry* 83 (2015): 335–338.

39. Z. Siroma, N. Fujiwara, S.-i. Yamazaki, M. Asahi, T. Nagai, and T. Ioroi, "Multi-Rail Transmission-Line Model as an Equivalent Circuit for Electrochemical Impedance of a Porous Electrode," *Journal of Electroanalytical Chemistry* 878 (2020): 114622.

40. Z. Siroma, N. Fujiwara, S. I. Yamazaki, M. Asahi, T. Nagai, and T. Ioroi, "Mathematical Solutions of Comprehensive Variations of a Transmission-Line Model of the Theoretical Impedance of Porous Electrodes," *Electrochimica Acta* 160 (2015): 313–322.

41. U. Tröltzsch and O. Kanoun, "Generalization of Transmission Line Models for Deriving the Impedance of Diffusion and Porous Media," *Electrochimica Acta* 75 (2012): 347–356.

42. J. Bisquert, G. Garcia-Belmonte, F. Fabregat-Santiago, and A. Compte, "Anomalous Transport Effects in the Impedance of Porous Film Electrodes," *Electrochemistry Communications* 1 (1999): 429–435.

43. M. Schalenbach, Y. E. Durmus, H. Tempel, H. Kungl, and R.-A. Eichel, "Double Layer Capacitances Analysed With Impedance Spectroscopy and Cyclic Voltammetry: Validity and Limits of the Constant Phase Element Parameterization," *Physical Chemistry Chemical Physics* 23 (2021): 21097–21105.

44. R. W. Bosch, "Electrochemical Impedance Spectroscopy for the Detection of Stress Corrosion Cracks in Aqueous Corrosion Systems at Ambient and High Temperature," *Corrosion Science* 47 (2005): 125–143.

45. I. D. Raistrick, "Impedance Studies of Porous Electrodes," *Electrochimica Acta* 35 (1990): 1579–1586.

46. W. Schmickler, *Electrochemical Theory: Double Layer* (Amsterdam, The Netherlands: Elsevier Inc., 2014).

47. R. Parsons, "Electrical Double Layer: Recent Experimental and Theoretical Developments," *Chemical Reviews* 90 (1990): 813–826.

48. L. Knijff, M. Jia, and C. Zhang, "Electric Double Layer at the Metal-Oxide/Electrolyte Interface," *Elsevier Encyclopedia of Solid-Liquid Interfaces* 1 (2024): 567–575.

49. S. L. Medway, C. A. Lucas, A. Kowal, R. J. Nichols, and D. Johnson, "In Situ Studies of the Oxidation of Nickel Electrodes in Alkaline Solution," *Journal of Electroanalytical Chemistry* 587 (2006): 172–181.

50. B. E. Conway and W. G. Pell, "Double-Layer and Pseudocapacitance Types of Electrochemical Capacitors and Their Applications to the Development of Hybrid Devices," *Journal of Solid State Electrochemistry* 7 (2003): 637–644.

51. A. M. Sahadevan, K. Gopinadhan, C. S. Bhatia, and H. Yang, "Parallel-Leaky Capacitance Equivalent Circuit Model for MgO Magnetic Tunnel Junctions," *Applied Physics Letters* 101 (2012): 162404.

52. M. Simic, A. K. Stavrakis, and G. M. Stojanovic, "A Low-Complexity Method for Parameter Estimation of the Simplified Randles Circuit With Experimental Verification," *IEEE Sensors Journal* 21 (2021): 24209–24217.

53. S. S. Madani, E. Schaltz, and S. K. Kær, "A Review of Different Electric Equivalent Circuit Models and Parameter Identification Methods of Lithium-Ion Batteries," *ECS Transactions* 87 (2018): 23–37.

54. V. Uskoković, "A Historical Review of Glassy Carbon: Synthesis, Structure, Properties and Applications," *Carbon Trends* 5 (2021): 100116.

55. W. Ryden and A. Lawson, "Temperature Dependence of the Resistivity of RuO2 and IrO2," *Physics Letters A* 26 (1968): 209–210.

56. T. R. Jow and J. P. Zheng, "Amorphous Thin Film Ruthenium Oxide as an Electrode Material for Electrochemical Capacitors," *Materials Research Society Symposium – Proceedings* 393 (1995): 433–438.

57. D. A. McKeown, P. L. Hagans, L. P. L. Carette, A. E. Russell, K. E. Swider, and D. R. Rolison, "Structure of Hydrous Ruthenium Oxides: Implications for Charge Storage," *Journal of Physical Chemistry B* 103 (1999): 4825–4832.

58. A. Mazzarolo, M. Curioni, A. Vicenzo, P. Skeldon, and G. E. Thompson, "Anodic Growth of Titanium Oxide: Electrochemical Behaviour and Morphological Evolution," *Electrochimica Acta* 75 (2012): 288–295.

59. J. Pouilleau, D. Devilliers, F. Garrido, S. Durand-Vidal, and E. Mahé, "Structure and Composition of Passive Titanium Oxide Films," *Materials Science and Engineering B* 47 (1997): 235–243.

60. D. Mardare, C. Baban, R. Gavrila, M. Modreanu, and G. I. Rusu, "On the Structure, Morphology and Electrical Conductivities of Titanium Oxide Thin Films," *Surface Science* 507–510 (2002): 468–472.

61. M. V. Diamanti and M. P. Pedeferri, "Effect of Anodic Oxidation Parameters on the Titanium Oxides Formation," *Corrosion Science* 49 (2007): 939–948.

62. M. E. G. Lyons, R. L. Doyle, I. Godwin, M. O. Brien, and L. Russell, "Hydrous Nickel Oxide: Redox Switching and the Oxygen Evolution Reaction in Aqueous Alkaline Solution," *Journal of the Electrochemical Society* 159 (2012): H932–H944.

63. D. S. Hall, D. J. Lockwood, C. Bock, and B. R. MacDougall, "Nickel Hydroxides and Related Materials: A Review of their Structures, Synthesis and Properties," *Proceedings. Mathematical, Physical, and Engineering Sciences* 471 (2014): 20140792.

64. S. Cherevko, S. Geiger, O. Kasian, et al., "Oxygen and Hydrogen Evolution Reactions on Ru, RuO2, Ir, and IrO2 Thin Film Electrodes in Acidic and Alkaline Electrolytes: A Comparative Study on Activity and Stability," *Catalysis Today* 262 (2016): 170–180.

Supporting Information

Additional supporting information can be found online in the Supporting Information section.